Journal of Electronic Materials (2022) 51:4446–4455
https://doi.org/10.1007/s11664-022-09690-9

ORIGINAL RESEARCH ARTICLE

Computational Analysis of Structural, Electronic, Magnetic and Optical Properties of $MgTM_2O_4$ (TM = Fe, V) Spinels

M. Hassan[1] · Mamoona Muazzam[1] · Taharh Zelai[2] · Q. Mahmood[3,4] · Bakhtiar Ul Haq[5]

Received: 10 November 2021 / Accepted: 29 April 2022 / Published online: 21 May 2022

Abstract

The electronic behavior, ferromagnetism and optical characteristics of $MgTM_2O_4$ (TM = V, Fe) cubic spinels are investigated using the full-potential linearized augmented plane wave (FP-LAPW) approach, which involves concepts of density functional theory. The calculated band structures reveal half-metallic behavior in MgV_2O_4 and a ferromagnetic semiconducting nature in $MgFe_2O_4$. Moreover, the density of states (DOS) reveals that the magnetism results from the strong hybridization between Fe/V-3*d* and O-2*p* states, due to which Fe/V magnetic moments are reduced because magnetic moments appear at Mg and O sites. Hence, the spinels have importance for spintronic applications. The ferromagnetic phase stability is confirmed by the values of released energy, which are consistent with the computed values of the crystal field and exchange energies. The dielectric constant and refractive index values are large for MgV_2O_4 but small for $MgFe_2O_4$ due to their half-metallic and semiconducting nature, respectively. The blueshift of the absorption spectrum makes the spinels attractive for optical applications. The electrical and thermal conductivity are also computed using BoltzTraP code, and potential energy conversion applications are suggested.

Keywords Half-metallic ferromagnetism · DFT-based material simulation · crystal field energy · exchange mechanism · dielectric behavior

Introduction

Among the various materials that play a vital role in the development of science and technology, spinels are the subject of immense interest as magnetic materials. Spinels are minerals that are composed of aluminum, magnesium, iron and manganese oxides, which are widely distributed in the earth's crust, moon rocks and meteorites.[1] Because of their high stability over a wide pressure and temperature range, spinels are present in many igneous and metamorphic rocks.[2] Spinel crystals exhibit space group 227-Fd3m and have a general structural formula AB_2O_4, where the divalent A and trivalent B cations are tetrahedrally and octahedrally coordinated, respectively.[3] $MgFe_2O_4$ and MgV_2O_4 are magnetic oxide spinels that have interesting electromagnetic and magnetic properties. The *n*-type cubic $MgFe_2O_4$ spinel exhibits a soft magnetic nature.[4] The face-centered cubic (FCC) close-packed spinel structure with chemical formula AB_2O_4 has eight formula units, where the oxygen ions involve 32 e-sites (depicting the anionic locations), while A and B atoms occupy the 8a and 16d locations. The octahedral and tetrahedral sites are produced in the unit cell by the FCC close packing of O ions.[5]

Because of their low cost and high electromagnetic response over a large frequency range, spinel ferrites are attractive candidates for a large array of technological applications.[6] The small dielectric and magnetic losses and large

✉ M. Hassan
mahmood.physics@pu.edu.pk

1 Materials Growth and Simulation Laboratory, Department of Physics, University of the Punjab, Quaid-i-Azam Campus, Lahore 54590, Pakistan

2 Department of Physics, Faculty of Science, Jazan University, Jazan, Saudi Arabia

3 Basic and Applied Scientific Research Center, Imam Abdulrahman Bin Faisal University, P.O. Box 1982, Dammam 31441, Saudi Arabia

4 Department of Physics, College of Science, Imam Abdulrahman Bin Faisal University, P.O. Box 1982, Dammam 31441, Saudi Arabia

5 Advanced Functional Materials and Optoelectronics Laboratory (AFMOL), Department of Physics, Faculty of Science, King Khalid University, P.O. Box 9004, Abha, Saudi Arabia

resistivity make magnesium ferrite suitable for microwave device applications.[7] They can also be used in the fields of catalysis, sensing and magnetic technologies, among others.[8] Recently, ferrite nanoparticles have attained great achievements in different fields.[9–14] Different growth methods have been used to prepare and study the properties of spinel oxides.[13,15–20] Among these applied methods, the choice of the appropriate method is based on the ability to provide a final product with uniform composition,[21] because the properties of magnetic spinels are significantly influenced by the ionic distribution.[22] This also suggests the effectiveness and usefulness of theoretical computational methodologies.

$MgFe_2O_4$ nanoparticles prepared by chemical beneficiation of iron ore were found to exhibit dielectric behavior.[23] By using the polymeric precursor method, $MgFe_2O_4$ pigment stabilized as a single phase was studied at low temperature and showed reflection to a reddish-yellow color within 600–650 nm.[24] Similarly, the microstructure and humidity-sensing properties of $MgFe_2O_4$ ferrites were investigated under the influence of Sn and Mo substitutions.[25] The nanocrystalline structure of $MgFe_2O_4$ was analyzed using x-ray diffraction. The most important Rietveld refinement technique and atomic pair distribution investigation showed that the nanocrystalline ferrite had limited structural coherence and a large degree of disorder. This structural information was used to explain the unusual magnetic behavior demonstrated.[26] The band gap of the $FeAl_2O_4$ spinel structure theoretically calculated using the generalized gradient approximation (GGA) and GGA+U methods was found to be consistent with the literature.[27] Similarly, in another experimental report, $MgFe_2O_4$ was prepared using a combustion reaction. The single phase elucidated using x-ray diffraction exhibited average crystallite size between 11.24 nm and 57.91 nm.[28] The hydrothermal growth of $NiFe_2O_4$/carbon nanotube compounds showed great purity and uniform particle size.[29] Despite the number of experimental reports on $MgFe_2O_4$, no comprehensive work on the theoretical computation of the physical properties exists in the literature. Similarly, MgV_2O_4 has not been well explored either experimentally or theoretically. The stabilized cubic phase and the magnetic properties exhibited by MgV_2O_4 and $Mg(V_{0.85}Al_{0.15})_2O_4$ have been explored experimentally, and a magnetic order up to 65 K has been reported.[30] Furthermore, an experimental study reported that MgV_2O_4 exhibited highly coupled lattice, spin and orbital degrees of freedom and a trigonal distortion at room temperature.[31] $MgFe_2O_4$ nanopowder prepared using a co-precipitation route confirmed a single cubic phase as observed from the measured x-ray diffraction (XRD) pattern. The saturation magnetization was recorded by a vibrating-sample magnetometer (VSM).[32] Tian et al. prepared $MgFe_2O_4$/metal–organic framework materials using a solvothermal method for organic dye removal. $MgFe_2O_4$ demonstrated excellent magnetic responsivity and fast absorption.[33] In the present work, we demonstrate that the electronic structure, magnetism and optical characteristics of MgV_2O_4 and $MgFe_2O_4$ spinels computed after the application of the modified Becke–Johnson (mBJ) potential are quite accurate. The investigations of the magnetic and optical characteristics suggest that these spinels may find use in novel spintronic and optical device applications.

Method of Calculation

The most versatile all-electron WIEN2k code based on the full-potential linearized augmented plane wave (FP-LAPW) method was used to simulate the spinel oxides.[34] To evaluate the exact Hamiltonian for accurate measurement of the ground-state energy and subsequently the structural properties, we used the Perdew–Burke–Ernzerhof generalized gradient approximation (PBE-GGA).[35,36] The exact electronic nature was calculated to determine the precise band gap by employing the mBJ potential,[37] because this potential yields a computed band gap consistent with the experiments.[38–40] Spin–orbit coupling (SOC) was also included in the calculations to attain accurate results. The electronic configurations for the Mg ($3s^2 2p^6$), Fe ($4s^2 3d^6$), V ($4s^2 3d^3$) and O ($2s^2 2p^4$) atoms were used to study the exchange mechanism.[41] Because the selection of k-points is very important for energy convergence, we apply a $13 \times 13 \times 13$ k-mesh after testing a number of k-meshes for the best execution of the computations, as the energy of the system remains invariant for further higher-order k-meshes.[42] Additionally, the value of the muffin-tin radius (R_{MT}) multiplied by the reciprocal lattice wave vector (K_{max}) was set as 10, while the value of G_{max} was taken as 9. Energy convergence up to 10^{-2} mRy was permitted, while employing an iterating sequence. The R_{MT} values taken for Mg, V, Fe and O were 1.8 a.u., 2.0 a.u., 2.05 a.u. and 1.76 a.u., respectively. For optimization, a 5% reduction in R_{MT} was chosen. The electrical and thermal conductivity were computed using BoltzTraP code.[43]

Results and Discussion

Structural and Thermodynamic Stability

The magnesium-based spinel oxides (MgX_2O_4) were found to exhibit a face-centered cubic (FCC) phase (*Fd3m-227*). The spinel (cubic) structure comprises a total of 56 atoms, consisting of 8, 16 and 32 Mg, Fe/V and O atoms, respectively. The Mg atoms occupy tetrahedral sites (8a) with atomic locations (1/8, 1/8, 1/8). The Fe/V atoms occupy octahedral sites (16d) with atomic sites (1/2, 1/2, 1/2), while the 32 oxygen atoms are associated with a parameter u that defines their locations

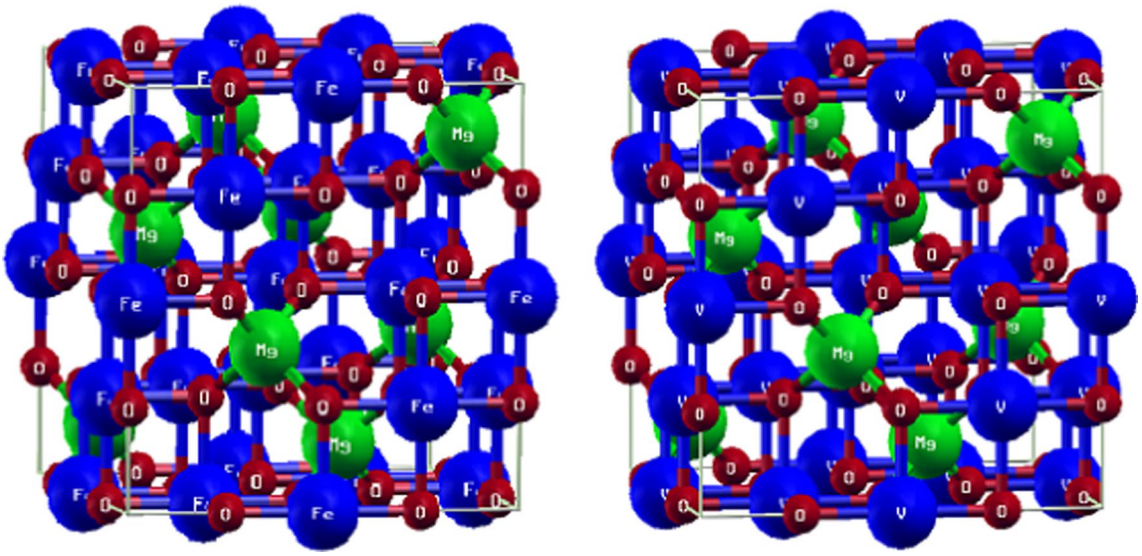

Fig. 1 Structures for both spinel oxides.

Table I The lattice constant a_o (Å), bulk modulus B_o (GPa), Curie temperature (T_C) and enthalpy of formation H_f (eV) determined for both spinels.

Compound	a_o (Å)	B_o (GPa)	T_C (k)	H_f (eV)
MgV_2O_4	6.035	185	330	−2.70
$MgFe_2O_4$	6.050	170	341	−2.26

in the spinel oxides. Therefore, the eight FCC unit cells of anions use 32 oxygen atoms (8×4 = 32) because of four tetrahedrons. The electronic structures computed for the MgV_2O_4 and $MgFe_2O_4$ spinels are presented in Fig. 1. Various parameters at the ground state are shown in Table I, including the lattice constant [a_0 (Å)] and bulk modulus B_0. These two parameters, extracted from the structural optimization curves, are found to be inversely linked, because MgV_2O_4 has larger B_0 and smaller a_0 as compared with that for $MgFe_2O_4$.

To determine the ferromagnetic (FM) state stability, the ground-state energies in the ferromagnetic (FM), paramagnetic (PM) and antiferromagnetic (AFM) states were calculated and are presented in Fig. 2a and b. The lower energy values for the FM state relative to the PM and AFM states indicate that the FM states are stable. The positive values of the energy difference between the FM and AFM states are listed in Table I.[44] FM state stability is also confirmed using the computed formation energy (ΔH_f), which is elucidated using the relation:

$$\Delta H_f = E_{Total}(V/Fe_lMg_mO_n) - lE_{V/Fe} - mE_{Mg} - nE_O \quad (1)$$

Here, $E_{Total}(V/Fe_lMg_mO_n)$, $E_{V/Fe}$, E_{Mg} and E_O represent the total energy of the spinel and energy for the crystals of the

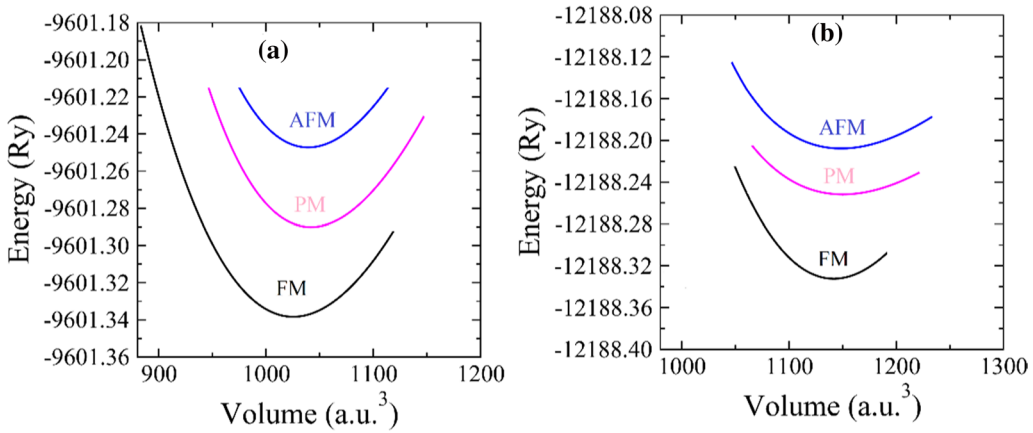

Fig. 2 The optimized energy–volume curves for (a) MgV_2O_4 and (b) $MgFe_2O_4$ in the FM, PM and AFM states.

respective elements. The negative sign of the computed formation energy indicates that spinel formation results in greater released energy, demonstrating the high thermodynamic stability of the cubic spinel in the FM state. The Curie temperature (T_C) is predicted using a classical approach according to the Heisenberg model: $T_C = 2\Delta E/3xK_B$, where K_B and X are the Boltzmann constant and doping concentration of transition metal ions which has been taken as unity in the un-doped spinel.[45] The Curie temperature (see Table I) determined for the spinels exhibits above room-temperature ferromagnetism (RTFM), which makes them potential candidates for spintronic applications.

Electronic Properties

The band structure (BS) is calculated for both MgV_2O_4 and $MgFe_2O_4$ spinels using the PBE-GGA functional and mBJ potential, with respect to the spin-polarized nature, as shown in Fig. 3. MgV_2O_4 exhibits half-metallic ferromagnetic characteristics after computation using either the PBE-GGA or mBJ functional, which occurs because spin-up and spin-down channels exhibit a metallic and insulating nature, respectively. In the spin-up channel, the Fermi level (E_F) crossing the valence state reveals that holes are available for conduction, while the spin-down channel shows a Fermi level within the band gap that illustrates an insulting nature. On the other hand, the BS for $MgFe_2O_4$ shows semiconducting and metallic behavior in the spin-up and spin-down channels, respectively, when computed using PBE-GGA. However, with the use of the mBJ potential, both channels exhibit a semiconducting nature, and hence, ferromagnetic semiconducting behavior becomes quite attractive for practical applications in novel devices. The metallic and semiconducting nature of both MgV_2O_4 (metallic for up spin) and $MgFe_2O_4$ (metallic for down spin only for PBE-GGA) may be justified due to the odd number of electrons in the V 3*d* states and even number of electrons in Fe 3*d* states. The use of the mBJ potential is found to improve the band gap, as apparent from Fig. 3. The electronic states move away from the Fermi level, resulting in enhanced band gap for the semiconducting channels. MgV_2O_4 exhibits a gap energy of 2.80 eV for the spin-down channel when the PBE-GGA functional is employed, which improves to 3.90 eV when the mBJ potential is applied. For MgV_2O_4, this gap is 3.50 eV for the spin-up channel when computed using the PBE-GGA functional, and it improves to 6.34 eV when the mBJ potential is used. In Fig. 3, the energy differences between the maxima of the valence bands and minima of the conduction bands for both channels are also labelled, because these energy differences directly reflect exchange energies induced due to hybridization.

The spin polarization (P) for MgV_2O_4 and $MgFe_2O_4$ was computed using $P = (N_\downarrow - N_\uparrow/N_\downarrow + N_\uparrow) \times 100$, where $N_\downarrow$ and $N_\uparrow$ are the states present at Fermi energy (E_F) for the

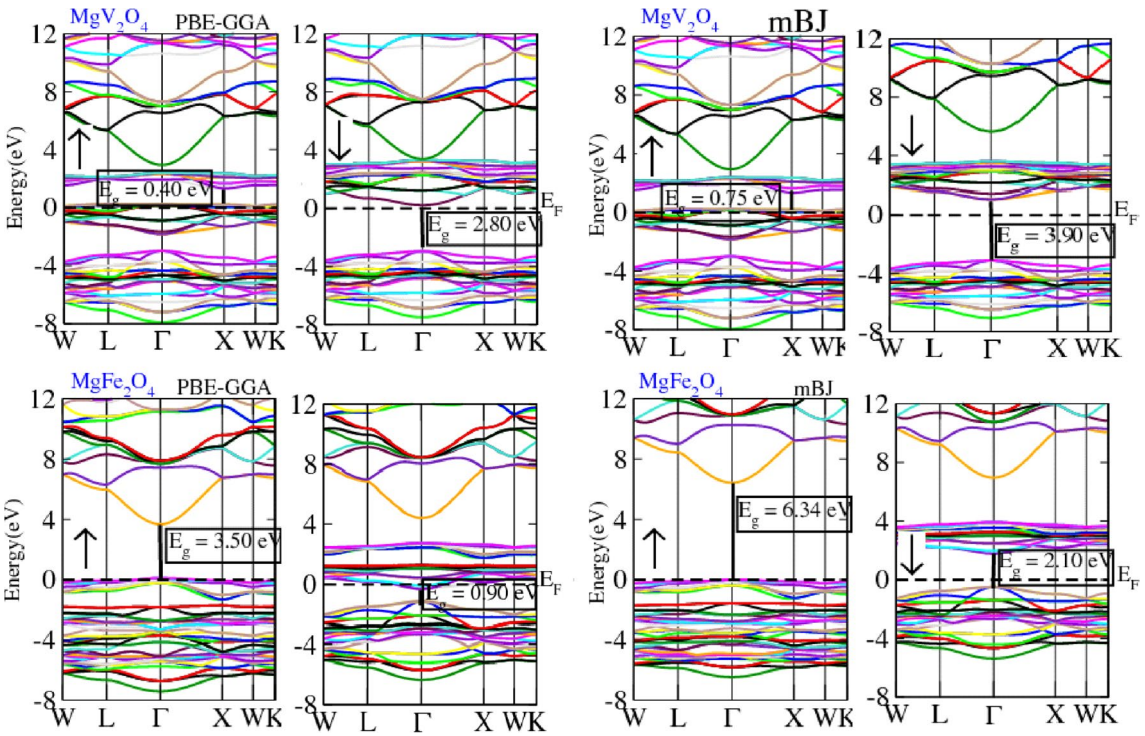

Fig. 3 Spin-polarized band structures calculated for MgX_2O_4 (X = V, Fe) using the mBJ potential.

respective spin channels. It is revealed that MgV_2O_4 exhibits 100% spin polarization after computations by both the PBE-GGA and mBJ potential, because the spin-up and spin-down channels show metallic and insulating behavior, respectively. On the contrary, $MgFe_2O_4$ reveals P =100% when computed using the PBE-GGA and P = 0% when the mBJ potential is employed, which evidences a shift from half-metallic to ferromagnetic semiconducting behavior due to the choice of exchange correlation functional.[46,47] The integer and fractional values of the total magnetic moment might be due to half-metallic and ferromagnetic semiconducting behaviors, respectively.

To further illustrate the reasons that the stabilized ferromagnetic state arises, the density of states for the spinels and individual constituent elements are computed using the mBJ potential and plotted in Fig. 4a and b. The total density of states (TDOS) indicates that the half-metallic ferromagnetic state is stabilized in MgV_2O_4, while the ferromagnetic semiconducting nature of $MgFe_2O_4$ is evident, and similar results are observed from the calculated BS plots. The shifting of states around $E_F$lower in the spin-up and spin-down channels occurs due to the splitting of the V/Fe 3*d* states that reduces the total energy of the spinels to stabilize the ferromagnetism.[48] Moreover, the partial density of states (PDOS) of V/Fe, Mg and O shows that the major contribution to the exchange mechanism around the E_F comes from V/Fe 3*d* states, with minor involvement of the O 2*p* and Mg 4*s* states for both spin channels. The O 2*p* and Mg 4*s* states contribute significantly within the energy range of −4 eV to −7 eV and do not contribute to the exchange process because these are the filled core states. However, the V/Fe 3*d* states within −2 eV to 3 eV around E_F actively hybridize with the O 2*p* states to induce ferromagnetism. Furthermore, the octahedral and tetrahedral environments of O ions split the V/Fe 3*d* states into doublet (e_g) and triplet (t_{2g}) states, which is due to the crystal field energy for both spin channels of

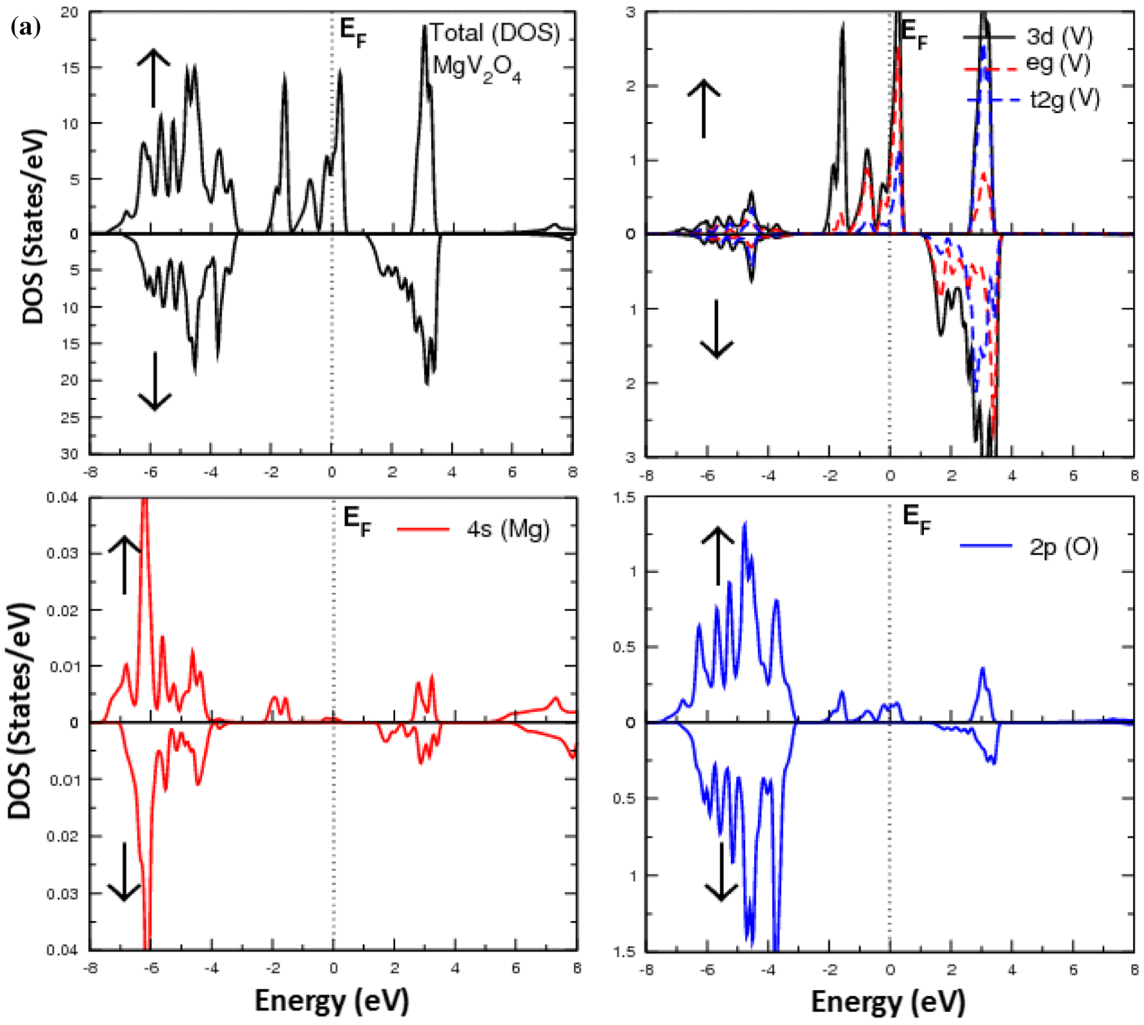

Fig. 4 (a) Total (TDOS) and partial density of states (PDOS) computed for MgV_2O_4 after applying the mBJ potential. (b) TDOS and PDOS computed for $MgFe_2O_4$ after applying the mBJ potential.

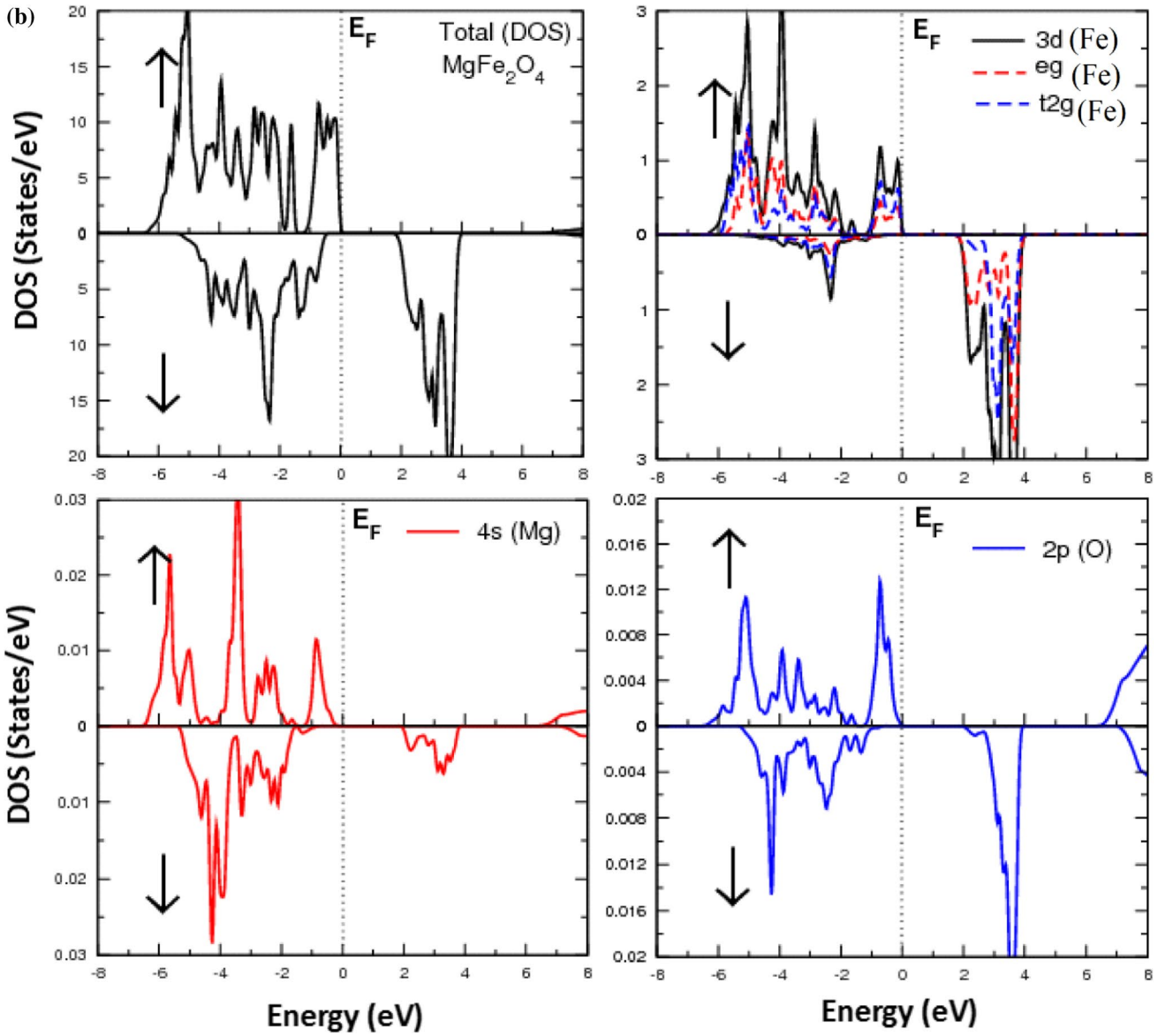

Fig. 4 (continued)

the spinels. The e_g states split into d_{x2-y2} and d_{z2} substates, while t_{2g} states split into d_{xy}, d_{xz} and d_{yz} substates. The crystallographic environment of O increases the energy of the d_{x2-y2} and d_{z2} substates in comparison with the d_{xy}, d_{xz}, and d_{yz} substates in both spin channels. We computed the crystal field energy for the up ($\Delta_{CF}^{\uparrow} = t_{2g}^{\uparrow} - e_g^{\uparrow}$) and down ($\Delta_{CF}^{\downarrow} = t_{2g}^{\downarrow} - e_g^{\downarrow}$) spin channels.[49] The difference between $\Delta_{CF}^{\uparrow}$ and $\Delta_{CF}^{\downarrow}$ can be employed to determine the crystal distortion defined as the Jahn-Teller energy (Δ_{JT}). The comparison of the crystal distortion and the exchange energies [Δx (d) and Δx (pd)] can also be employed to evaluate the stability of the ferromagnetic state (see Table II). The $\Delta x(d)$ is the direct exchange energy parameter calculated from the energy difference of the 3d states in both spin channels, while Δx (pd) is the indirect exchange energy computed from the valence band edge splitting in both channels. The lower value of Δ_{JT} relative to the exchange energies indicates stable ferromagnetism.[50] The negative Δx (pd) illustrates that the energy is released from the spinels due to strong underlying p-d hybridization (see Table II), which lowers the energy of the system and indicates the stability of the dominant ferromagnetic behavior. Furthermore, the double exchange mechanism may be responsible for mediating ferromagnetism in the MgV_2O_4 half-metallic spinel, while the superexchange mechanism might be responsible for inducing ferromagnetism in the semiconducting $MgFe_2O_4$ spinel.

Table II Various parameters extracted from the computed electronic properties for both spinels.

Compound	ΔE_C (eV)	Δx (d)	(Δ_{JT})	Δx (pd)	$N_o\,\alpha$	$N_o\,\beta$
MgV_2O_4	−2.23	2.849	−3.369	−3.109	2.468	−1.998
$MgFe_2O_4$	0.414	−1.709	0.141	−1.068	−0.723	−0.311

Magnetic Properties

To further investigate the magnetic properties of MgV_2O_4 and $MgFe_2O_4$, the calculated total and partial magnetic moments of the spinels and constituent elements (Mg, O and V/Fe), respectively, are presented in Table III. The total magnetic moments are mainly contributed by the V/Fe atoms; however, interstitial sites also contribute to the total magnetic moment, which occur due to the hybridization phenomena, while small magnetic moments are also exhibited due to Mg and O. Such small magnetic moments induced at Mg and O are basically shifted from the V/Fe sites because of the considerable *p-d* hybridization, which evidences the dominant role of the electronic spin instead of the clustering of the magnetic atoms. Such sharing of magnetic moments is further elucidated by computing the spin density plots as presented in Fig. 5. The yellow flowered shapes around the V/Fe atoms show their main contribution to the total magnetic moment, while shifting of small magnetic moments toward Mg and O sites is also apparent.[51]

Table III Total and partial magnetic moments.

Compound	Total	Mg-site	O-site	V/Fe-site	Int-site
MgV_2O_4	3.0000	0.00435	0.01238	1.76706	0.82401
$MgFe_2O_4$	5.0000	0.01853	0.38093	3.99353	0.78024

The ferromagnetism can also be analyzed by the valence (ΔE_v) and conduction band edge splitting (ΔE_c), which occurs due to *s-d* and *p-d* exchange mechanisms, respectively. These exchange energies can be written in terms of exchange constants $N_o\alpha$ and $N_o\beta$ according to the relations $N_o\alpha = \Delta E_C/x\langle S\rangle$, $N_o\beta = \Delta E_V/x\langle S\rangle$, where x is the concentration of V/Fe, which is taken as 1 in the present case.[52] For MgV_2O_4, $N_o\alpha$ is positive and $N_o\beta$ is negative, indicating antiparallel coupling, while for $MgFe_2O_4$, both exchange constants $N_o\alpha$ and $N_o\beta$ are negative, indicating parallel coupling. In both spinels, $N_o\beta$ (which measures the valence band edge splitting) remains negative, indicating a decrease in energy and improvement in the stability of the ferromagnetic state. The changes in the sign of $N_o\alpha$ might be caused by quantum confinement effects that influence the density of states in both spin channels.[53] The exchange constants also distinguish the underlying mechanism determining the half-metallic or semiconducting ferromagnetic nature. The mechanism responsible for the half-metallic ferromagnets is double exchange, while for ferromagnetic semiconductors, super-exchange is most appropriate.[54,55]

Optical Parameters

The optical behaviors of half-metallic and semiconducting ferromagnets depend upon the intra-band (within the band) transitions and inter-band (conduction to valence band)

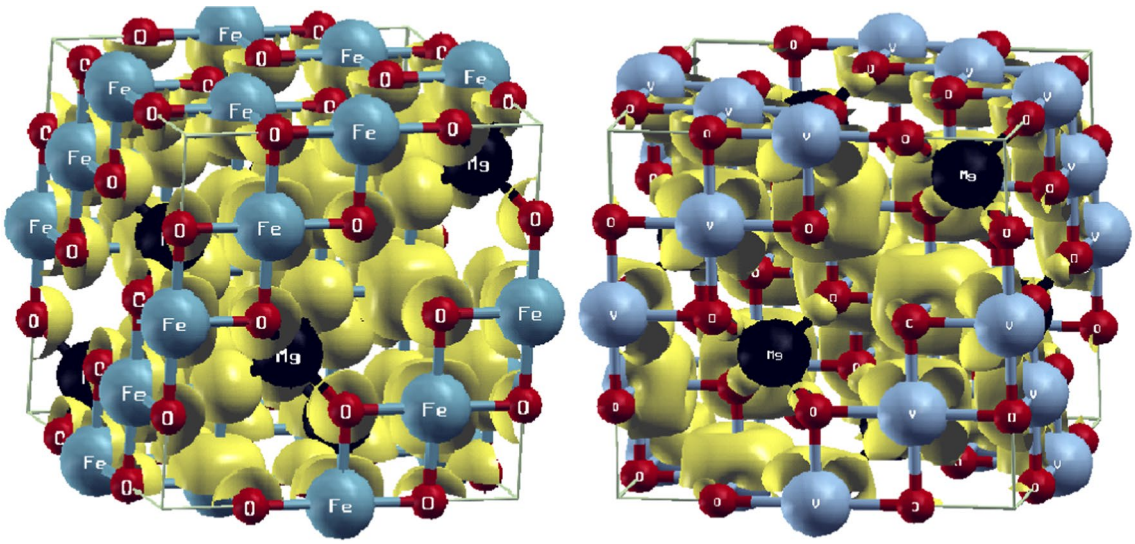

Fig. 5 Spin charge density plots computed for both compounds (Color figure online).

transitions, respectively. For metals, the dielectric constants have large values, small absorption, and large polarization and dispersion, while semiconductors have small values of dielectric constants, large absorption and small dispersion in the low-frequency range of the spectrum. For computing the optical properties, the OPTIC program was employed and Kramers–Kronig relations were used.[56,57] The optical behaviors of MgV_2O_4 and $MgFe_2O_4$ spinel oxides are studied by computing the complex dielectric constant $\varepsilon(\omega) = \varepsilon_1(\omega) + i\varepsilon_2(\omega)$, where $\varepsilon_1(\omega)$ and $\varepsilon_2(\omega)$ represent the real and imaginary parameters of $\varepsilon(\omega)$, respectively, which are related according to Kramers-Kronig relations.[56,57] The refraction is also calculated for the energy range 0–15 eV and is presented in Fig. 6.

Both the real $\varepsilon_1(\omega)$ and imaginary $\varepsilon_2(\omega)$ parts of $\varepsilon(\omega)$ calculated for MgV_2O_4 and $MgFe_2O_4$ spinels, as presented in Fig. 6a and b, show the dispersion/polarization and absorption of light, respectively. The static value of $\varepsilon_1(\omega)$ is very high (at zero frequency) for MgV_2O_4 because of its half-metallic behavior, while for $MgFe_2O_4$, it is small because of the ferromagnetic semiconducting behavior (as evident from the computed electronic properties). The value of $\varepsilon_1(\omega)$ falls sharply from a constant value and becomes negative at 0.5 eV, indicating the reflection of incident radiation, after which it increases a small amount to become constant, indicating that the dispersion of light is suppressed, as shown in Fig. 6a. For $MgFe_2O_4$, the $\varepsilon_1(\omega)$ remains constant up to 7 eV and then increases to a peak value at 8 eV, indicating that light is dispersed and polarizes at the resonance frequency and drops to the minimum value. Moreover, the $\varepsilon_1(0)$ and band gap E_g determined from the BS are not consistent with Penn's model, which might be due to the exchange split process of the interacting states. The violation of Penn's model for MgV_2O_4 may be due to its metallic nature and strong p–d hybridization.[58,59] The $\varepsilon_2(\omega)$ indicates the absorption of light by the spinel. The plots of $\varepsilon_2(\omega)$ for MgV_2O_4 and $MgFe_2O_4$ are presented in Fig. 6a and b. For MgV_2O_4, the $\varepsilon_2(\omega)$ shows strong absorption at low energy, which is due to the half-metallic nature of the spinel. On the other hand, $MgFe_2O_4$ does not exhibit maximum absorption until the incident energy exceeds the critical value, which is due to the band gap of this semiconducting spinel. The strong absorption peak at low energy is due to intra-band transitions in the half-metallic MgV_2O_4, which also exhibit low absorption around 6eV. In contrast, the semiconducting/insulating nature of $MgFe_2O_4$ results in a blue shift in the computed absorption edge that appears at around 7.0 eV. The refractive index $n(\omega)$ represents a transparent nature, while the extinction coefficient $k(\omega)$ describes absorption exhibited by the spinels to the impinging light. The computed $n(\omega)$ and $k(\omega)$ are given in Fig. 6c and d, which indicate the real and imaginary dielectric constant and are linked according to the relations $n^2 - k^2 = \varepsilon_1(\omega)$ and $2nk = \varepsilon_2(\omega)$, respectively.[60–62] Moreover, the zero-frequency limit of refractive index $n(0)$ and $\varepsilon_1(0)$ fulfill the condition $n_o^2 = \varepsilon_1(0)$, as evident from Fig. 6. It is clear that the computed optical parameters are consistent with the electronic properties of both spinels (half-metallic and semiconducting), which demonstrates the accuracy of the computations.

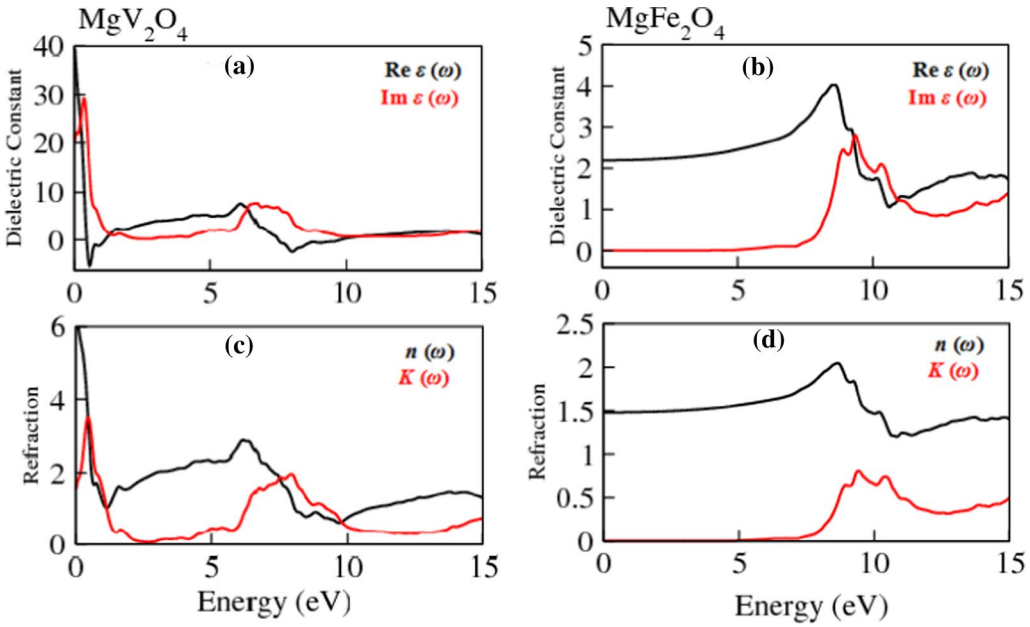

Fig. 6 The dielectric function, refractive index and extinction coefficient for MgV_2O_4 (a, c) and $MgFe_2O_4$ (b, d) calculated using the mBJ potential.

Electrical and Thermal Conductivity

The electrical conductivity (σ/τ) and electronic thermal conductivity (κ_e/τ) of MgX_2O_4 (X = V, Fe) are computed and presented in Fig. 7a and b, respectively. The electrical conductivity σ/τ increases with increasing temperature for both spinels, as evident from Fig. 7a, because at high temperature more free carriers are available for conduction. The σ/τ for MgV_2O_4 (a half-metallic ferromagnet) is higher than that for $MgFe_2O_4$ (a semiconducting ferromagnet) because the V-based spinel has lower activation energy than the Fe-based spinel for free electron conduction. Similarly, electronic thermal conductivity (κ_e/τ) increases with temperature, as evident from Fig. 7b, because thermal conduction is also increased due to these free electrons. The κ_e/τ is higher for MgV_2O_4 than $MgFe_2O_4$ at lower temperature, but it is lower at higher temperature, which might be due to the comparatively large thermal agitation of the lattice sites in MgV_2O_4 that impedes the thermal flow due to free electrons. Furthermore, the electronic thermal conductivity is highly sensitive to the crystal dimension, crystalline quality and nature of the stabilized phase. Generally, the major requirements for designing the most efficient thermoelectric material are a higher value of electrical conductivity and lower electronic thermal conductivity. As evident from Fig. 7a and b, the magnitude of σ/τ is higher than κ_e/τ, which could be important not only for spintronic devices but also for thermoelectric device applications.[63]

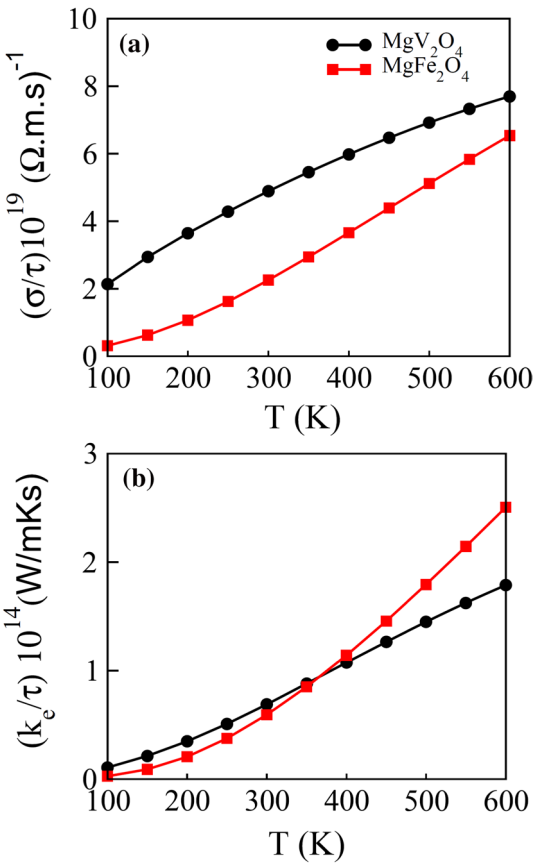

Fig. 7 The computed (a) electrical conductivity and (b) electronic thermal conductivity of MgX_2O_4 (X = V, Fe).

Conclusions

The electronic and optical properties of $MgTM_2O_4$ (TM = V, Fe) magnetic spinels were calculated for potential applications in modern devices. The MgV_2O_4 was found to be half-metallic ferromagnet, while $MgFe_2O_4$ is a ferromagnetic semiconductor. The greater stability of the FM state than the AFM state was confirmed by the release of more energy in the FM state. The negative enthalpy of formation indicates that spinels are thermodynamically stable in the FM state. The comparatively larger exchange energy than the crystal field and Jahn–Teller energy confirm a stable ferromagnetic nature governed by spin interactions. The negative sign of indirect exchange energy reveals energy lowering to stabilize ferromagnetism in the spinels. The strong *p–d* hybridization across the Fermi level results in half-metallic and semiconducting ferromagnetism due to the double-exchange and super-exchange mechanisms in MgV_2O_4 and $MgFe_2O_4$, respectively. Finally, the high dispersion and transparency and minimum absorption of MgV_2O_4 shows its metallic behavior, while absorption of light in the ultraviolet region for $MgFe_2O_4$ with lower dispersion and transparency makes it appropriate for novel optical device fabrication. The computed thermoelectric parameters reveal that the greater values of electrical conductivity than thermal conductivity are well suited for spintronic and energy conversion applications.

Funding The author M. Hassan (Mahmood-ul-Hassan) is also thankful to University of the Punjab for the financial assistance of this work through the Faculty Research Grant Program for the years 2022–2023. The author Bakhtiar Ul Haq extends his appreciation to the Deanship of Scientific Research at King Khalid University for funding his work through the Research Groups Program under Grant No. R.G.P. 2/186/43.

Data Availability The datasets generated during and/or analyzed during the current study are available from the corresponding author on reasonable request.

Conflict of interest The authors declare that they have no conflict of interest.

References

1. A.K. Singh, A. Dhillon, T.D. Senguttuvan, and A.M. Siddiqui, *Int. J. Current Eng. Technol.* 4, 6 (2014).

2. S. Klemme, H.C. O'Neill, W. Schnelle, and E. Gmelin, *Am. Mineral.* 85, 1686 (2000).
3. B. Viswanathan and V.R.K. Murthy, Narosa Publishers (1990).
4. R. Sepahvand and R. Mohamadzade, *J. Mater. Sci. Appl.* 2, 1564 (2011).
5. K.E. Sickafus, J.M. Wills, and N.W. Grimes, *J. Am. Ceram. Soc.* 82, 3279 (1999).
6. G. Dixit, J.P. Singh, R.C. Srivastava, H.M. Agarwal, and R.J. Chaudhary, *Adv. Mater. Lett.* 3, 21 (2012).
7. D. Bahadur, *Bull. Mater. Sci.* 15, 431 (1992).
8. S.V. Bangale, D.R. Patil, and S.R. Bamane, *Arch. Appl. Sci. Res.* 3, 506 (2011).
9. V.G. Harris, A. Geiler, and Y. Chen, *J. Magn. Magn. Mater.* 321, 2035 (2009).
10. Y. Qu, H. Yang, and N. Yang, *Mater. Lett.* 60, 3548–3552 (2006).
11. N. Kasapoglu, B. Birsoz, and A. Baykal, *Cent. Eur. J. Chem.* 5, 570 (2007).
12. S.W. Cao, Y.J. Zhu, G.F. Cheng, and Y.H. Huang, *J. Hazard.* 171, 431 (2009).
13. Y.L. Liu, Z.M. Liu, and Y. Yang, *Sens. Actuator B Chem.* 107, 600 (2005).
14. M. Koledintseva, J. Drewniak, Y. Zhang, J. Lenn, and M. Thoms, *J. Magn. Magn. Mater.* 321, 730 (2009).
15. A.I. Turkin and V.A. Drebushchak, *J. Cryst. Growth* 265, 165 (2004).
16. T. Sasaki et al., *J. Supercrit. Fluids* 53, 92 (2010).
17. H. Aono, H. Hirazawa, T. Naohara, and T. Maehara, *Appl. Surf. Sci.* 254, 2319 (2008).
18. A. Pradeep, P. Priyadharsini, and G. Chandrasekaran, *J. Magn. Magn. Mater.* 320, 2774 (2008).
19. V. Šepelák, D. Baabe, D. Mienert, F.J. Litterst, and K.D. Becker, *Scr. Mater.* 48, 961 (2003).
20. Y. Huang, Y. Tang, J. Wang, and Q. Chen, *Mater. Chem. Phys.* 97, 394 (2006).
21. Y. Zhang and G.C. Stangle, *J. Mater. Res.* 9, 1997 (1994).
22. N. Kaur, S. Sharma, S. Kaur, and H. Nayyar, *Arch. Agron. Soil Sci.* 60, 1593 (2014).
23. K.S. Rane, V.M.S. Verenkar, and P.Y. Sawant, *Bull. Mater. Sci.* 24, 323 (2001).
24. R.A. Candeia, M.A.F. Souza, M.I.B. Bernardi, S.C. Maestrelli, I.M.G. Santos, A.G. Souza, and E. Longo, *Mater. Res. Bull.* 41, 183 (2006).
25. C. Doroftei, E. Rezlescu, N. Rezlescu, and P.D. Popa, *J. Optoelectron. Adv. Mater.* 8, 1012 (2006).
26. M. Gateshki, V. Petkov, S.K. Pradhanb, and T. Vogt, *J. Appl. Crystallogr.* 38, 772 (2005).
27. M. Khalid, S. Riaz, S. Naseem and M. Azam, Theoretical study of spinel structure of $FeAl_2O_4$ using density functional theory, in *Proceedings of The 2014 World Congress on Advances in Civil, Environmental and Materials Research (ACEM'14)*, August 24-28, BEXCO, Busan, Korea. http://www.i-asem.org/acem14_publication.html
28. S. Da Dalt and C.P. Bergmann, Viña del Mar, Chile (2010).
29. Y.Q. Liu and L. Gao, *Carbon* 43, 47 (2005).
30. H. Mamiya, M. Onoda, T. Furubayashi, J. Tang, and I. Nakatani, *J. Appl. Phys.* 81, 5289 (1997).
31. E.M. Wheeler, B. Lake, A.T.M.N. Islam, M. Reehuis, P. Steffens, T. Guidi, and A.H. Hill, *Phys. Rev. B* 82, 140406 (2010).
32. F. Naaz, H.K. Dubey, C. Kumari, P. Lahiri, and S.N. Appl, *Sci.* 2, 808 (2020).
33. H. Tian, J. Peng, T. Lv, C. Sun, and H. He, *J. Solid State Chem.* 257, 40 (2018).
34. P. Blaha, K. Schwarz, G.K.H. Madsen, D. Kvasnicka, and J. Luitz, Technische Universitat Wien, Austria (2001).
35. S.M. Alay-e-Abbas, S. Nazir, K.M. Wong, A. Shaukat, and U. Schwingenschlogl, *EPL* 106, 27003 (2014).
36. K.M. Wong, S.M. Alay-e-Abbas, Y. Fang, A. Shaukat, and Y. Lie, *J. Appl. Phys.* 114, 034901 (2013).
37. F. Tran and P. Blaha, *Phys. Rev. Lett.* 102, 226401 (2009).
38. N.A. Noor, S.M. Alay-e-Abbas, M.U. Sohaib, S.M.G. Abbas, and A. Shaukat, *J. Magn. Magn. Mater.* 374, 164 (2015).
39. D.J. Singh, *Phys. Rev. B* 82, 205102 (2010).
40. M. Sajjad, H.X. Zhang, N.A. Noor, S.M. Alay-e-Abbas, A. Shauka, and Q. Mahmood, *J. Magn. Magn. Mater.* 343, 177 (2013).
41. P. Hohenberg and W. Kohn, *Phys. Rev.* 136, 86 (1964).
42. H.J. Monkhorst and J.D. Pack, *Phys. Rev. B* 13, 5188 (1976).
43. G. K. Madsen, D. J. Singh, BoltzTraP. A code for calculating band-structure dependent quantities. *Comput. Phys. Commun.* 175, 67 (2006).
44. Q. Mahmood, M. Hassan, M.A. Faridi, B. Sabir, G. Murtaza, and A. Mahmood, *Curr. Appl. Phys.* 16, 549 (2016).
45. Q. Mahmood, S.M. Alay-e-Abbas, M. Yaseen, A. Mahmood, M. Rashid, and N.A. Noor, *Super. Cond. Magen.* 29, 1 (2016).
46. C. Wen and S. Yan, *J. Appl. Phys.* 107, 043913 (2010).
47. H.S. Saini, M. Singh, A.H. Reshak, and M.K. Kashyap, *J. Magn. Magn. Mater.* 331, 1 (2013).
48. M. Sajjad, H.X. Zhang, N.A. Noor, S.M. Alay-e-Abbas, A. Shaukat, and Q. Mahmood, *J. Magn. Magn. Mater.* 343, 177 (2013).
49. A. Walsh, S.H. Wai, Y. Yan, M.M. Al-Jassim, and J.A. Turner, *Phys. Rev. B* 76, 16511 (2007).
50. Q. Mahmood and M. Hassan, *J. Alloys Compd.* 704, 659 (2017).
51. T. Dietl, *Semicond. Sci. Technol.* 17, 377 (2002).
52. Q. Mahmood, S.M. Alay-e-Abbas, M. Hassan, and N.A. Noor, *J. Alloys Compd.* 688, 899 (2016).
53. S. Sanvito, P. Ordejon, and N.A. Hill, *Phys. Rev. B.* 63, 165206 (2001).
54. R.D. McNorton, T.M. Schuler, and J.M. MacLaren, *Phys. Rev. B* 78, 075209 (2008).
55. R.A. Stern, T.M. Schuler, J.M. MacLaren, D.L. Ederer, V. Perez-Dieste, and F.J. Himpsel, *J. Appl. Phys.* 95, 7468 (2004).
56. G. Marius, Springer, Berlin (2010), pp. 775–776
57. D. Koller, F. Tran, and P. Blaha, *Phys. Rev. B.* 83, 195134 (2011).
58. D. Penn, *Phys. Rev.* 128, 2093 (1962).
59. W. Benstaalia, S. Bentata, A. Abbad, and A. Belaidi, *Mater. Sci. Semi. Proc.* 16, 231237 (2013).
60. M.A. Khan, A. Kashyap, A.K. Solanki, T. Nautiyal, and S. Auluck, *Phys. Rev. B* 48, 16974 (1993).
61. R. Khenata et al., *Solid State Commun.* 136, 120 (2005).
62. W. Benstaalia, S. Bentata, A. Abbad, and A. Belaidi, *Mater. Sci. Semicond. Proc.* 16, 231 (2013).
63. T.I. Al-Muhimeed, G.M. Mustafa, A.A. AlObaid, A. Mera, K. Shahzadi, M. Mana AL-Anazy, and Q. Mahmood, *Eur. Phys. J. Plus* 137, 299 (2022).